Computational Mechanics
https://doi.org/10.1007/s00466-021-02136-9

ORIGINAL PAPER

A hybrid lattice Boltzmann-molecular dynamics-immersed boundary method model for the simulation of composite foams

Mohammadmehdi Ataei[1,2] · Erfan Pirmorad[1] · Franco Costa[3] · Sejin Han[4] · Chul B. Park[1] · Markus Bussmann[1]

Received: 15 August 2021 / Accepted: 21 December 2021

Abstract
Small fillers (e.g., carbon fibers) are commonly added to polymer foams to create composite foams that can improve foam properties such as thermal and electrical conductivity. Understanding the motion and orientation of fillers during the foaming process is crucial because these can affect the properties of composite foams significantly. In this work, a hybrid lattice Boltzmann method-molecular dynamics-immersed boundary method model is presented for simulating the foaming process of polymer composites. The LBM model resolves the foaming process, and the MD model accounts for filler dynamics. These two solvers are coupled by a direct forcing IBM. This solver can simulate composite foaming processes involving many bubbles and filler particles, including rigid and deformable 3D particles, and rigid, deformable, and fragile fibers. The solver relaxes most simplifying assumptions of earlier polymer composite models, allowing for a better understanding of filler motion and interaction with growing bubbles.

Keywords Lattice Boltzmann method · Fiber reinforced · Polymer foam composites · Molecular dynamics · Numerical methods

1 Introduction

Polymer foams are usually created by dissolving gas in a polymer melt and then inducing a sudden pressure drop, which initiates gas bubble nucleation and growth. The growing bubbles (cells) form a cellular structure with numerous intriguing functional properties. Polymer foam composites made by the addition of rod-like fillers (such as carbon fibers [60]) and solid fillers (such as metallic particles and conducting polymer particles [45]) have been widely studied, and have been used in a variety of industries in recent years. The addition of fibers and wires strengthens the foam, and allows for specific properties and functions, such as electromagnetic interference, to emerge, that are of great industrial interest in shielding [11,35,38,53,55,80], bipolar fuel cell plates [1,31,43], high-dielectric charge storage, and tunable conductivity conductors [13,64].

The distribution and orientation of fillers are determining factors responsible for the intriguing physical properties of polymer composites. Previous research has shown that cell growth realigns fillers and increases filler connectivity, which can aid in the formation of connective networks among fillers [42,44,66,73,74]. Ameli et al. [3,4] shows that foaming can increase the electrical conductivity of PP/MWCNT composites up to an optimum void fraction, after which the conductivity decreases, and in another work, demonstrates that in foam injection molding of PP/MWCNT nanocomposites, a 10-fold increase in dielectric permittivity can be achieved due to the arrangement of MWCNT between adjacent cells [5] . On the other hand, Rizvi et al. [54] shows that foaming can also result in reduction of electrical conductivity due to unknown factors.

Therefore, a better understanding of filler interaction and movement in foaming processes during cell growth is critical for the design and control of the distribution and orientation of fillers, resulting in materials with improved properties. Several studies have been conducted to extract relationships

✉ Markus Bussmann
markus.bussmann@utoronto.ca

1 Department of Mechanical and Industrial Engineering, University of Toronto, 5 King's College Rd, Toronto, ON M5S 3G8, Canada

2 Present Address: Autodesk Research, 661 University Ave, Toronto, ON M5G 1M1, Canada

3 Autodesk, Inc., 259-261 Colchester Rd., Kilsyth, VIC 3137, Australia

4 Autodesk, Inc., 217 North Aurora Street, Ithaca, NY 14850, USA

Published online: 09 January 2022

between the geometric orientation of fillers and the physical properties of composite materials [12,26,27,37,40,50,74,81]. For example, Folgar and Tucker [21] introduced a simulation model to evaluate fiber orientation using a fiber orientation distribution function for simple flows, and Advanli et al. [2] utilized moments of that distribution function to accelerate the computations [21]. Jack et al. [32] developed a neural network-based closure model that can be used to calculate fiber orientation in short-fiber polymer composites. In these and similar models (e.g., [9,10,15,41,71]), fiber interactions are thought to be due to volume-averaged effects, and fibers are modeled as individual rigid ellipsoids in a Newtonian fluid using the Jeffery equation. Commercial software such as Moldflow and Digimat have also been used to study fiber orientation in injection molding [22,24,30,51,59,61]; a comparison of the fiber orientation models in Moldflow can be found in [70].

Despite the rich literature on fiber orientation in composite materials, little research has been done to model the motion and interactions of fillers during foaming [60,72]. A basic analytical model by Shaayegan et al. [60] considers the change in the radius of a single spherical bubble on the rotation and translation of a single fiber. The bubble growth is not explicitly modeled, effect of the fiber on the bubble is ignored, the fiber can only translate radially, and its rotation is restricted to about it mid-point. Finally, Wang et al. [72] extended this model to two growing cells to evaluate the effects of cell size, filler weight, and relative position of the filler with respect to the cells on the displacement and orientation of the fiber. While these analytical models contribute to an understanding of the interaction of filler rotation and movement due to growing cell(s), their applicability is restricted due to their simplifications.

In this paper, we present a multi-physics fluid-structure solver for modeling foaming with a variety of solid fillers of different geometries, including rigid, flexible, and fragile fibers, and arbitrarily-shaped 3D fillers. Unlike previous models, foaming with many growing bubbles is modeled, accounting for bubble growth, interaction, and coalescence, and the fillers can move freely in 2D and 3D spaces. To the best of our knowledge, this model is the most detailed for the simulation of polymer foam composites, and relaxes most previous simplifying assumptions.

The governing equations of the foaming process, and of filler dynamics, are solved separately in their entirety, with no restrictive simplifications. The lattice Boltzmann method (LBM) is used to resolve the fluid and gas dynamics in the polymer melt; to model the filler dynamics, a molecular dynamics (MD) approach is used. A multi-direct forcing immersed boundary method (IBM) is used to couple the fluid and solid solvers [29]. Both LBM and MD are parallelized across many processors, which allows for dramatic speed up of large-scale simulations with many bubbles and fillers.

In the following sections, the numerical methodology will be presented, followed by a number of validation cases. Finally, we demonstrate the capabilities of the model by simulating 2D and 3D foaming processes with various fillers.

2 Methodology

2.1 Foaming model

In this work the foaming process is modeled using our previously developed LBfoam [7] software, a 2D/3D free surface lattice Boltzmann solver for foaming simulation. LBfoam solves an advection–diffusion equation coupled to a fluid flow equation, to capture dissolved gas diffusion into bubbles, subject to a Henry's law boundary condition at bubble-liquid interfaces. LBfoam accounts for the disjoining pressure between bubbles, surface tension, film drainage, and bubble dynamics and coalescence; an improved model that avoids the majority of the simplifications seen in the commonly used Cell Model [6,8,69]. A volume-of-fluid (VOF) method is used for interface capturing. The LBM method is suitable for simulating foaming, because it enables simple implementation of the Henry's law boundary condition at bubble-liquid interfaces (that are immersed in the domain and arbitrarily shaped) via a population reconstruction step, as well as efficient parallelization of the simulation for large-scale simulations. Furthermore, LBM is a desired choice for fast and efficient fluid-structure simulation using the Immersed Boundary Method [18–20].

In the following, the LBfoam model for foaming is briefly explained; more detail can be found in [7].

2.1.1 Free surface lattice Boltzmann method (LBM)

The lattice Boltzmann equation is a reduced form of the Boltzmann kinetic equation, that originates from statistical mechanics, and is widely used for fluid flow simulation. The original Boltzmann equation can be expressed as:

$$\frac{\partial f}{\partial t} + \boldsymbol{\xi} \cdot \nabla f + \frac{\mathbf{g}}{\rho} \cdot \frac{\partial f}{\partial \boldsymbol{\xi}} = \hat{C} \tag{1}$$

where f is the particle probability distribution, ρ is the density, $\boldsymbol{\xi}$ is the particle velocity, $\mathbf{g}$ is the external force, and $\hat{C}$ is the collision kernel. The Boltzmann equation is discretized by introducing a set of discrete velocities leading to the lattice Boltzmann equation:

$$f_i(\mathbf{x} + \mathbf{e}_i, t+1) - f_i(\mathbf{x}, t) = \hat{C}_i(\mathbf{x}, t) \tag{2}$$

which can be decomposed into collision and streaming steps as:

$$\text{Collision: } f_i^c(\mathbf{x}, t) = f_i(\mathbf{x}, t) + \hat{C}_i(\mathbf{x}, t)$$
$$\text{Streaming: } f_i(\mathbf{x} + \mathbf{e}_i, t + 1) = f_i^c(\mathbf{x}, t)$$

where $f_i(\mathbf{x}, t)$ is a particle probability distribution function (PDF) at location $\mathbf{x}$ and time t, f_c^i denotes the post-collision PDF, and $\mathbf{e_i}$ are discrete lattice velocities which are expressed as follows for the simulation of a 3D fluid flow on a D3Q19 lattice:

$$\mathbf{e}_i = \begin{cases} (0,0,0) & i = 0 \\ (\pm 1,0,0),(0,\pm 1,0),(0,0,\pm 1) & i = 1,2,3,4,5,6 \\ (\pm 1,\pm 1,0),(\pm 1,0,\pm 1),(0,\pm 1,\pm 1) & i = 7,\ldots,18 \end{cases} \tag{3}$$

Through a Chapman–Enskog expansion, it can be shown that the lattice Boltzmann equation with the collision kernel $\hat{C}$ can be used to solve the incompressible Navier-Stokes equation [25]. The collision kernel $\hat{C}_i(\mathbf{x}, t)$ for isothermal systems (with external force contribution term F_i) is determined by the Bhatnagar–Gross–Krook (BGK) model [28] as follows:

$$\hat{C}(\mathbf{x}, t) = -\frac{1}{\tau}\left(f_i(\mathbf{x}, t) - f_i^{eq}(\mathbf{x}, t)\right) + F_i \tag{4}$$

where τ is the time interval between particle collisions, which is related to the kinematic viscosity ν by [28]:

$$\nu = c_s^2\left(\tau - \frac{1}{2}\right) \tag{5}$$

and F_i is calculated as:

$$F_i = w_i\left(1 - \frac{1}{2\tau}\right)\left(\frac{\mathbf{e}_i^\top \mathbf{u}}{c_s^4}\mathbf{e}_i - \frac{\mathbf{u} - \mathbf{e}_i}{c_s^2}\right)\cdot \mathbf{g} \tag{6}$$

where $\mathbf{g}$ is the external force density vector. The equilibrium probability distribution is given by:

$$f_i^{eq}(\rho, \mathbf{u}) = \rho w_i\left(1 + \frac{\mathbf{e}_i^\top \mathbf{u}}{c_s^2} + \frac{(\mathbf{e}_i^\top \mathbf{u})^2}{2c_s^4} - \frac{\mathbf{u}^2}{2c_s^2}\right) \tag{7}$$

where w_i are weight coefficients and c_s is the speed of sound. The macroscopic quantities ρ (density) and $\mathbf{u}$ (velocity) are calculated by summation of PDFs as follows:

$$\rho(\mathbf{x}, t) = \sum_{i=0}^{N} f_i \tag{8}$$

$$\mathbf{u}(\mathbf{x}, t) = \frac{1}{\rho}\left(\sum_{i=0}^{N} f_i \mathbf{e}_i + \frac{1}{2}\cdot \mathbf{g}\right) \tag{9}$$

The bounce-back scheme is used for particles colliding with walls to impose the no-slip boundary condition.

Liquid–gas interfaces are tracked by a scalar field that is equal to one in liquid cells, zero in gas cells, and between zero and one in interface cells. A full description of the interface capturing model can be found in [7].

2.2 Advection–diffusion

The dynamics of the dissolved gas within the liquid, and gas diffusion into growing bubbles, is taken into account by an advection–diffusion equation:

$$\frac{\partial c}{\partial t} + \nabla\cdot(c\mathbf{u}) = \nabla\cdot(D\nabla c) + q \tag{10}$$

c is the gas concentration and q is a source term for gas generation (e.g., due to a chemical reaction). A distribution function $g_i(\mathbf{x}, t)$ is used to solve the advection–diffusion equation:

$$g_i(\mathbf{x} + \mathbf{e}_i, t + 1) = g_i(\mathbf{x}, t) + \frac{1}{\tau_g}\left(g_i^{eq}(\mathbf{x}, t) - g_i(\mathbf{x}, t)\right) + w_i q \tag{11}$$

The diffusion constant is related to τ_g as $D = c_s^2\left(\tau_g - \frac{1}{2}\right)$. The gas concentration c is found by:

$$c(\mathbf{x}, t) = \sum_{i}^{N} g_i(\mathbf{x}, t) \tag{12}$$

The equilibrium distribution in the advection–diffusion equation is given by:

$$g_i^{eq}(\mathbf{x}, t) = w_i c(\mathbf{x}, t)\left(1 + \frac{\mathbf{e}_i^\top \mathbf{u}}{c_s^2}\right) \tag{13}$$

2.2.1 Disjoining pressure

A disjoining pressure Π acts between adjacent bubble interfaces to stabilize a foam. Π is a function of the distance between two bubbles d active up to a distance d_{max}:

$$\Pi = \begin{cases} 0 & d > d_{max} \\ k_\Pi\left(1 - \frac{d}{d_{max}}\right) & d < d_{max} \end{cases} \tag{14}$$

where k_Π is a constant.

2.3 Filler model

Molecular Dynamics (MD) is a numerical method often used in chemistry, biochemistry, and biophysics for simulation of interactions between a set of atoms, particles, or molecules

[14,17,23,34,36,48,52,58,63,78], based on a potential function U that defines the interaction between different particles. Given the potential function, internal forces acting on each particle are calculated as the gradient of the potential function. The total force on each particle $\mathbf{F}_i$ is the sum of internal $\mathbf{F}_i^{int}$ (e.g., due to elasticity) and external $\mathbf{F}_i^{ext}$ (e.g., hydrodynamic forces due to fluid-structure interaction) forces:

$$\mathbf{F}_i = \mathbf{F}_i^{int} + \mathbf{F}_i^{ext} \tag{15}$$

Numerical integration is used to calculate the motion of each particle using Newton's second law:

$$m_p \frac{d^2\mathbf{r}_i}{dt^2} = \mathbf{F}_i \tag{16}$$

where m_p is the mass of particle. By integrating the above equation twice, we can update particle velocity and position.

In the following sections, we discuss different potential functions that are used to model 2D fiber and 3D solid fillers that are made up of interacting particles. The LAMMPS [49] simulation package is used to calculate the filler dynamics; this is a powerful library written in C++ that includes many pre-defined functions for MD simulation, and a library of potential functions. LAMMPS is built as a shared library and incorporated into LBfoam through a C-style API. LBfoam serves as the "driver" and calls LAMMPS as an external library.

Note that the LAMMPS timestep δ_{tl} can vary from the LBfoam timestep δ_t. A smaller δ_{tl} is usually needed for a LAMMPS simulation to be stable. To accomplish this, for each δ_t, LBfoam invokes LAMMPS to advance for M timesteps where $M = \delta_t/\delta_{tl}$. For the simulations presented in this work M ranges from 2 to 10, ensuring that the velocity of each particle representing the fibers/solids not exceed $u_{lb} < 0.05$, where u_{lb} is the lattice velocity.

2.3.1 Fiber model

Fibers of length L_f are represented by a simple chain of n_a connected particles as shown in Fig. 1.

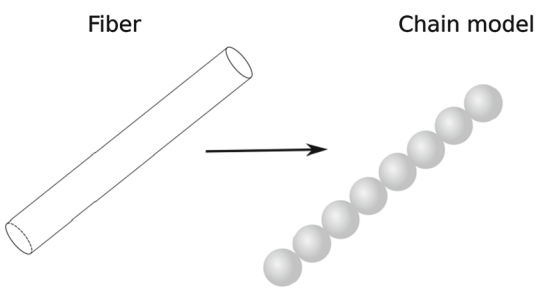

Fig. 1 Fibers (left) are modeled as chains of connected particles (right)

Since the area and volume of elastic fibers are negligible, only stretching and bending potentials are used to model the energy accumulated in the fiber structure due to these two deformation modes:

$$U_{\text{fiber}} = U_{\text{stretching}} + U_{\text{bending}} \tag{17}$$

A harmonic potential is used for $U_{\text{stretching}}$:

$$U_{\text{stretching}} = k_s(r_{ij} - r_{0,ij})^2 \tag{18}$$

where r_{ij} is the bond length for adjacent particles i and j, and $r_{0,ij}$ is the equilibrium bond distance between them [68], initially set to L_f/n_a. k_s is the stiffness constant related to the Young's modulus Y:

$$k_s = Y\frac{\pi a^2}{L_f} \tag{19}$$

where a is the radius of the fiber taken to be 0.2 μm in this work. Similarly, a harmonic bending potential is defined as:

$$U_{\text{bending}} = k_b(\theta_{ijk} - \theta_{0,ijk})^2 \tag{20}$$

where θ_{ijk} is the angle between three adjacent particles i, j, and k, $\theta_{0,ijk}$ is the equilibrium angle between them [68], and k_b is a constant.

To model fiber breakage and fragility, the bond between two particles is assumed to break with probability p^* if $r_{i,j} > r_{max,ij}$.

2.3.2 Coarse-grained membrane model for 3D fillers

The modeling of 3D solid fillers such as metallic particles and conducting polymer particles [45] is enabled by a coarse-grained (CG) membrane model [23,48,63] in which a group of particles connected together as a network is treated as a single entity, as shown in Fig. 2. This model is commonly used for MD simulation of larger molecules and particles [14, 17,34,78]. Area and volume harmonic potential functions are added to the stretching and bending potentials to control the rigidity of the solid and enforce a constant volume constraint, respectively:

$$U_{\text{membrane}} = U_{\text{stretching}} + U_{\text{bending}} + U_{\text{area}} + U_{\text{volume}} \tag{21}$$

The bending potential is given by the following function:

$$U_{\text{bending}} = \sum_{\text{adjacent } \alpha,\,\beta \text{ pair}} k_b[1 - cos(\theta_{\alpha,\beta} - \theta_0)] \tag{22}$$

where $\theta_{\alpha,\beta}$ and θ_0 are the instantaneous and initial dihedral angles between two adjacent triangular elements α and

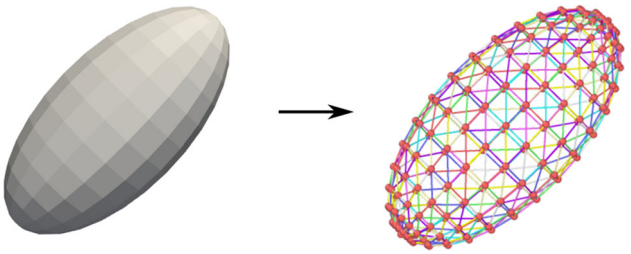

Fig. 2 Depiction of a coarse-grained membrane model for an ellipsoid that can be rigid or undergo deformation depending on the area and volume constraints

β, respectively. Conservation of the surface area and total volume are imposed by assigning the following harmonic potential functions:

$$U_{\text{area}} = \sum_{\text{k} \in \text{triangles}} \frac{k_d (A_k - A_{0,k})^2}{2A_{0,k}} + \frac{k_a (A_t - A_{0,t})^2}{2A_{0,t}} \quad (23)$$

$$U_{\text{volume}} = \frac{k_v (V - V_0)}{2V_0} \quad (24)$$

where k_d, k_a, and k_v are constants. A_k and A_t are the instantaneous surface area of the triangle k and the total area, respectively, and V is the volume of the object. Subscript zero indicates equilibrium values.

For the coarse-grained membrane model, the relations between the parameters of the model and continuum material properties such as the shear modulus can be derived through theoretical analysis of a hexagonal network of springs as explained in detail in [14,16,48]

Converting a triangular unstructured mesh into the LAMMPS data file format is challenging. For this reason, we have open-sourced the library that we developed for this task, Mesh2LAMMPS,[1] that converts a mesh file into a LAMMPS data file, and vice versa.

2.4 Particle–particle and particle–interface interaction

To avoid particles overlapping each other, a Morse potential is added to the potentials:

$$U_{\text{morse}} = k_m \left(e^{-2(r_{ij} - r_{0,ij})} - 2e^{(r_{ij} - r_{0,ij})} \right) \qquad r < r_{cut} \quad (25)$$

where r_{cut} is the cutoff, set equal to the lattice size, and $k_m = 4 \times 10^{-6}$.

Fiber-interface interaction is not directly modeled in this work. To prevent fibers from entering bubbles (within which the fluid flow is not modeled [7]), the momentum $\rho \mathbf{u}$ of interface cells in close proximity to particles is updated to $\rho \bar{\mathbf{u}}$, where $\bar{\mathbf{u}}$ is the average velocity of particles (in a 3×3 stencil around the interface cell) approaching the interface. As such, particles are slightly repelled from nearby interfaces.

[1] Freely available at https://github.com/mehdiataei/mesh2lammps.

2.5 Fluid–structure interaction: multi-direct forcing IBM

The coupling between fibers and/or particles interacting with the fluid flow is achieved through the immersed boundary method (IBM). In IBM, instead of physical boundaries, an additional external force is added to the momentum equation near the virtual boundary points to enforce the no-slip boundary condition. There are different methods for calculating the external force. The multi-direct forcing method of Inamuro [29] is used, that precisely satisfies the no-slip condition on moving boundaries through an iterative process.

The solid immersed boundary (IB) is represented by a set of Lagrangian points which overlap the Eulerian LBM grid. As shown in Fig. 3, the velocity of fluid flow at these Lagrangian points is interpolated from the Eulerian grid as follows:

$$\mathbf{u}\left(\mathbf{X}_k, t\right) = \sum_x \mathbf{u}(\mathbf{x}, t) W\left(\mathbf{x} - \mathbf{X}_k\right) \delta x^d \quad (26)$$

where $\mathbf{X_k}$ and $\mathbf{x}$ are the position vectors of the Lagrangian and Eulerian grid points respectively. d is dimensionality, and the Dirac function W for a three-dimensional system is defined as follows:

$$W(x, y, z) = \frac{1}{\delta x} w\left(\frac{x}{\delta x}\right) w\left(\frac{y}{\delta x}\right) w\left(\frac{z}{\delta x}\right) \quad (27)$$

where δx is lattice size and the smoothing function w is as proposed by Peskin [47]:

$$w(\mathbf{r}) = \begin{cases} \frac{1}{8}\left(3 - 2\,|\,r\,| + \sqrt{1 + 4\,|\,r\,| - 4r^2}\right) & \text{if } |\,r\,| \leq 1 \\ \frac{1}{8}\left(5 - 2\,|\,r\,| - \sqrt{-7 + 12\,|\,r\,| - 4r^2}\right) & \text{if } 1 \leq |\,r\,| \leq 2 \\ 0 & \text{if } |\,r\,| \geq 2 \end{cases} \quad (28)$$

Given the equations above, the IB force required to enforce the no-slip boundary condition is calculated by the following iterative algorithm:

Step 1 Initialize the body force on the Lagrangian points:

$$\mathbf{F}_0\left(\mathbf{X}_k, t\right) = \frac{\mathbf{v}_k\left(\mathbf{X}_k, t\right) - \mathbf{u}\left(\mathbf{X}_k, t\right)}{\delta t} \quad (29)$$

where $\mathbf{v}_k(\mathbf{X}_k, t)$ is the velocity of the Lagrangian points that make up the solid particles calculated and updated by the MD solver. $\mathbf{u}(\mathbf{X}_k, t)$ is the velocity of the fluid flow, computed by the LBM solver, interpolated to the Lagrangian grid points.

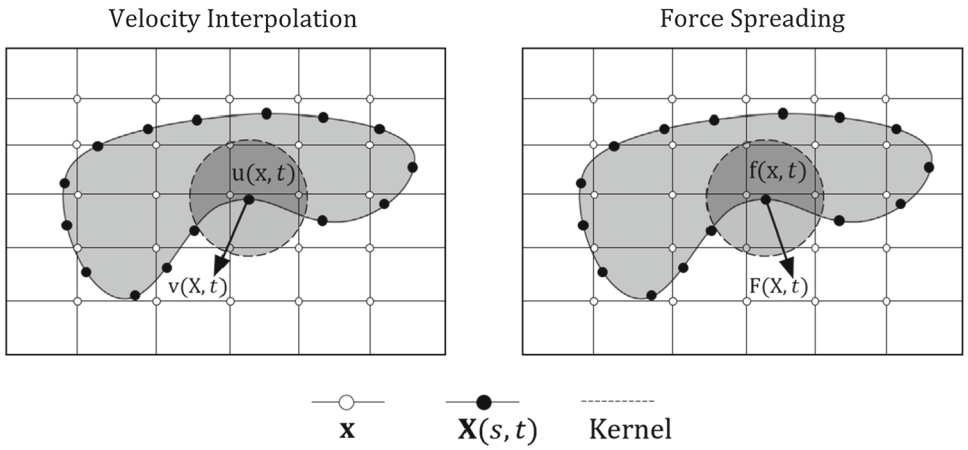

Fig. 3 Fluid-solid coupling through force and velocity interpolation between the Eulerian and Lagrangian grids. The solid immersed boundary (IB) can be non-stationary and flexible, and in 2D is described by $\mathbf{X}(s,t) : 0 \leq s \leq L_b$ curve, where L_b is the length of the immersed boundary

Intuitively, the external body force required to enforce the no-slip condition at the immersed boundary is proportional to the velocity difference between the solid body and fluid flow at the boundary points.

Step 2 Interpolate the force of the neighboring Eulerian grid points at the i-th iteration:

$$\mathbf{f}_i(\mathbf{x},t) = \sum_{\mathbf{X}_k} \mathbf{F}_i(\mathbf{X}_k,t) W(\mathbf{x}-\mathbf{X}_k) A_k \tag{30}$$

where A_k is the surface area of the Lagrangian point k.

Step 3 Correct the fluid flow velocity:

$$\mathbf{u}_i(\mathbf{x},t) = \mathbf{u}_i(\mathbf{x},t) + \mathbf{f}_i(\mathbf{x},t)\delta t \tag{31}$$

Step 4 Interpolate the corrected velocities at the Lagrangian grid points:

$$\mathbf{u}_i(\mathbf{X},t) = \sum_{x} \mathbf{u}_i(\mathbf{x},t) W(\mathbf{x}-\mathbf{X}_k)\delta x^d \tag{32}$$

Step 5 Update the force at the Lagrangian points located on the immersed boundary:

$$\mathbf{F}_{i+1}(\mathbf{X}_k,t) = \mathbf{F}_i(\mathbf{X}_k,t) + \frac{\mathbf{v}(\mathbf{X}_k,t) - \mathbf{u}_i(\mathbf{x}_k,t)}{\delta t} \tag{33}$$

Step 6 Return to step 2, and iterate until converged. This iterative process is repeated until

$$|\mathbf{F}_{i+1}(\mathbf{X}_k,t) - \mathbf{F}_i(\mathbf{X}_k,t))| / \mathbf{F}_i(\mathbf{X}_k,t) < 1 \times 10^{-2} \tag{34}$$

We discovered that three to four iterations are sufficient to achieve convergence. As a result, we limited the maximum number of iterations to six. The external forces on Lagrangian points calculated here are then input into the MD solver as $\mathbf{F}^{ext}$ to enforce the effect of the fluid flow on motion of the immersed bodies.

Figure 4 is a flowchart of the algorithm for the coupling of the fluid flow and the MD solver though the IBM.

3 Verification and validation

Validations of the LBM foaming code are given in [7], and so the validations presented here focus on the MD and IBM implementations.

3.1 Neutrally buoyant ellipsoid in a shear flow

The fluid-structure model is examined by considering the behavior of a buoyant ellipsoid in a shear flow, a test which is extensively used in the literature [39,57,67,77]. We use the formulation presented in [67]. As shown in Fig. 5, an ellipsoid with aspect ratio ψ is placed between two walls moving in opposite directions. The flow profile is given by $v_y = s(y - y_p)$, where s is the shear rate and v_y and y_p are the velocity and the center of the domain in the y-direction. Ellipsoid orientation versus the z-axis is given by ϕ_x and the angular velocity is ω_x. The computational domain is a cube of size $[0; \Omega_x] \times [0; \Omega_y] \times [0; \Omega_z]$ with periodic boundary conditions in the x and y directions. Different grid sizes were used based on the ratio $D/\delta x$, where δx is the cell size and $D = 2\kappa\psi^{-2/3}$ is the equivalent diameter of the ellipsoid, where κ is the largest principal half-axis of the ellipsoid. To prevent deformation, k_s, k_b, k_v and k_a were set to large values. At a small Reynolds number $Re = 4s\kappa^2/\nu << 1$ and an infinite confinement ratio Ω_y/κ, the analytical solution for the periodic motion of the ellipsoid can be found using the Jeffery orbit [33,67]. The period of the rotation is given by:

$$T = \frac{2\pi}{s}\left(\psi + \psi^{-1}\right) \tag{35}$$

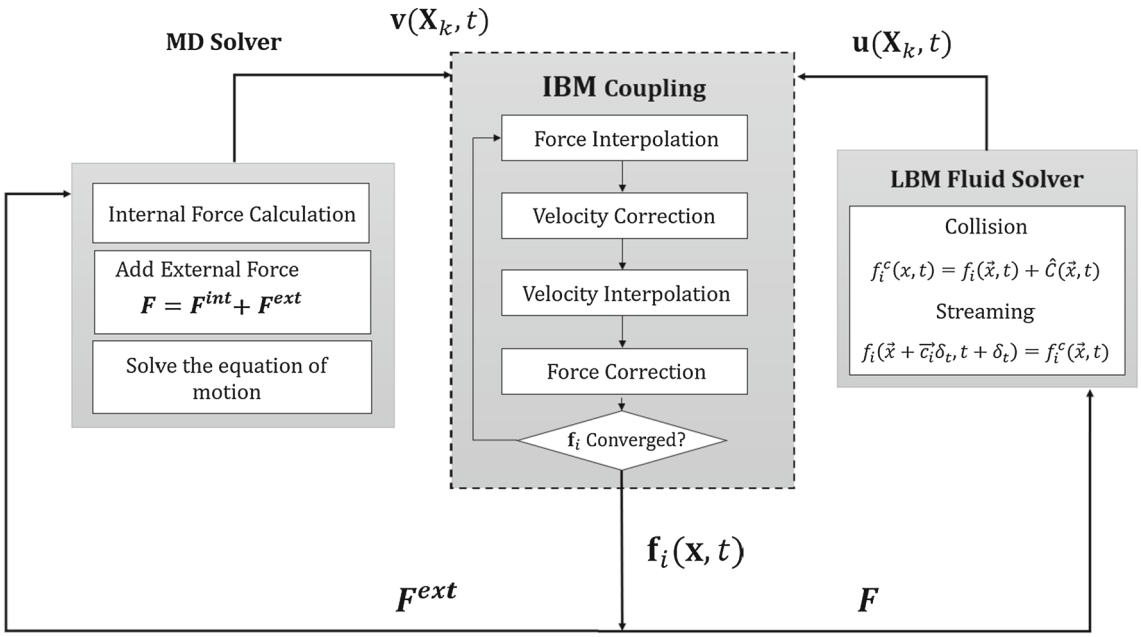

Fig. 4 The algorithm used to couple the LBM and MD solvers through IBM

and the motion of the ellipsoid is governed by:

$$tan(\phi_x) = \psi tan(\digamma t) \tag{36}$$

where $\digamma = 2\pi T^{-1}$. The angular velocity ω_x can be expressed as a function of ϕ_x:

$$\omega_x(\phi_x) = \psi^{-1}\digamma cos^2(\phi_x)\Big(\psi^2 + tan^2(\phi_x)\Big) \tag{37}$$

from which the maximum and minimum angular velocities can be found:

$$\omega_{max} = \frac{s\psi^2}{(1+\psi^2)} \tag{38}$$

$$\omega_{min} = \frac{s}{(1+\psi^2)} \tag{39}$$

Figure 6 shows results of the fully-developed periodic motion of an ellipsoid as a function of grid refinement. The Reynolds number is 0.3, $\psi = 2$, and the confinement ratio is held between 6 and 8. It can be seen that there is good agreement between the analytical and numerical solutions, and the agreement between the solutions improves with mesh refinement. As shown in Table 1, the simulation slightly underpredicts ω_{max} and slightly overpredicts ω_{min}; however, the difference decreases as $D/\delta x$ increases.

The order of convergence can be estimated as:

$$\mathcal{O} \approx \frac{\log(E)}{\log(D/\delta x)} \tag{40}$$

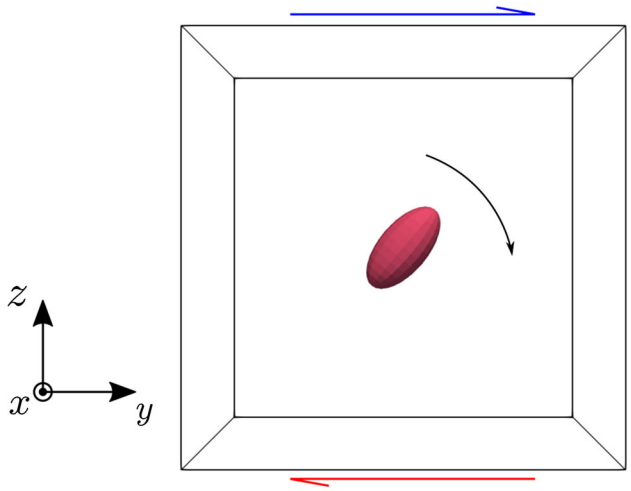

Fig. 5 Ellipsoid rotating periodically in a shear flow

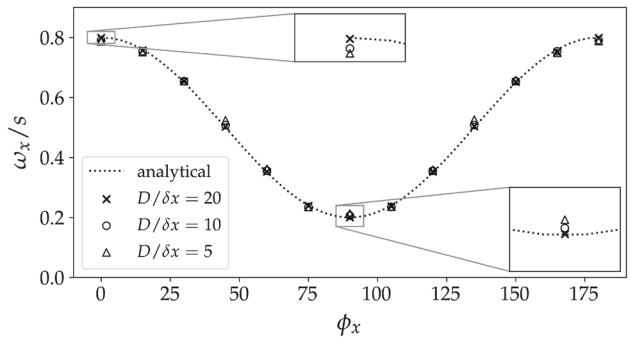

Fig. 6 ω_x/s versus ϕ_x compared to the analytical solution

Table 1 The errors of maximum and minimum values of ω_x on different grid sizes, versus the analytical model

$D/\delta x$	ω_{max}/s (%)	ω_{min}/s (%)
5	− 1.65	6.49
10	− 1.12	2.99
20	− 0.12	0.50

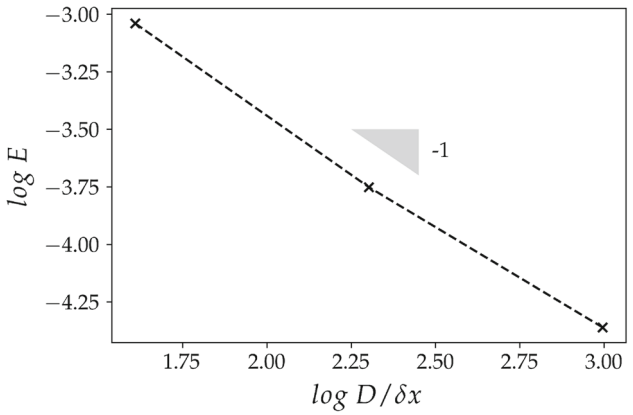

Fig. 7 Convergence based on the L2-norm

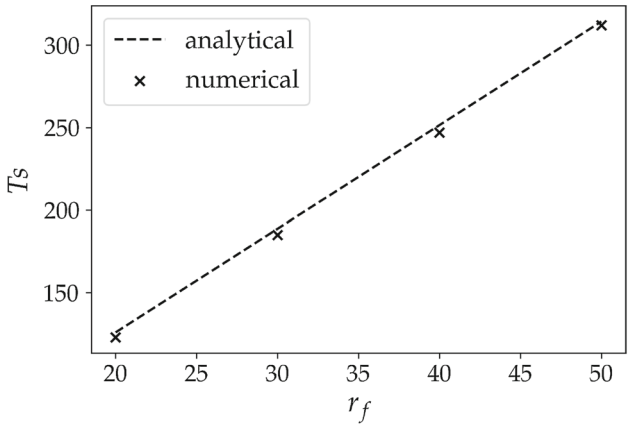

Fig. 8 Comparison of the Jeffery orbit prediction of Ts, and the results of the numerical model

Table 2 Simulation conditions for two cases used to reproduce the analytical results of Shaayegan et al. [60] using the numerical model presented here

Case #	α_0 (°)	R_0 (mm)	L_f (mm)
1	90	0.22	0.18
2	14.5	0.3	0.29

where $\mathcal{O}$ is the convergence order and E is the L2-norm of the error with respect to the analytical solution. The convergence of the error is shown in Fig. 7. Convergence is first-order, consistent with the result of [47].

3.2 Fiber rotation in a shear flow

We investigate the period of rotation T of a single rigid fiber in a shear flow, similar to that of Sect. 3.1. We set $k_s = k_b = 0.5$, which are sufficiently large to prevent deformation of the fiber. Analytically, the period of rotation T:

$$T = 2\pi(r_f + r_f^{-1})/s \tag{41}$$

where s is the shear rate and $r_f = L_f/2a$ is equal to the number of rigid spheres that comprise the fiber, as explained in [56,75,76]. Other conditions are similar to those of Sect. 3.1. As shown in Fig. 8, Ts increases almost linearly with r_f as predicted by the Jeffrey equation.

3.3 Fiber transition and rotation

The validity of the interaction between fibers and bubbles is addressed by comparing simulation results to the analytical model of Shaayegan et al. [60] for a single fiber and bubble pair, which describes the instantaneous fiber orientation and location as a function of an adjacent cell size, as shown in Fig. 9. In Fig. 9, R_0, R, and R_c are the initial location of the fiber, instantaneous location of the fiber, and the cell radius, respectively. The initial and instantaneous fiber angles are α_0 and α.

The analytical solution of Shaayegan et al. includes several simplifying assumptions. The bubble is assumed to remain spherical, the fiber only moves radially, the fiber angle α varies only around the fiber midpoint, and the fiber only rotates within the plane in which it resides. In this model, α is expressed as:

$$\alpha = arccos\left(\frac{2(A+B)}{L_f}\right) \tag{42}$$

where A and B are given by:

$$A = \left[(3V_0/16\pi) + ((3V_0/16\pi)^2 + (R_0^3 + R_c^3)^2)^{1/2}\right]^{1/3} \tag{43}$$

$$B = \left[(3V_0/16\pi) - ((3V_0/16\pi)^2 + (R_0^3 + R_c^3)^2)^{1/2}\right]^{1/3} \tag{44}$$

V_0 is the volume of the polymer envelope around the bubble, which is either a function of R_0 and α_0 (initial conditions) or R and α (instantaneous conditions) [60].

Table 2 presents the two cases that were simulated using the LBM-MD-IBM model, by placing a bubble and a fiber in a 3D domain of size 201 × 201 × 201, with the initial

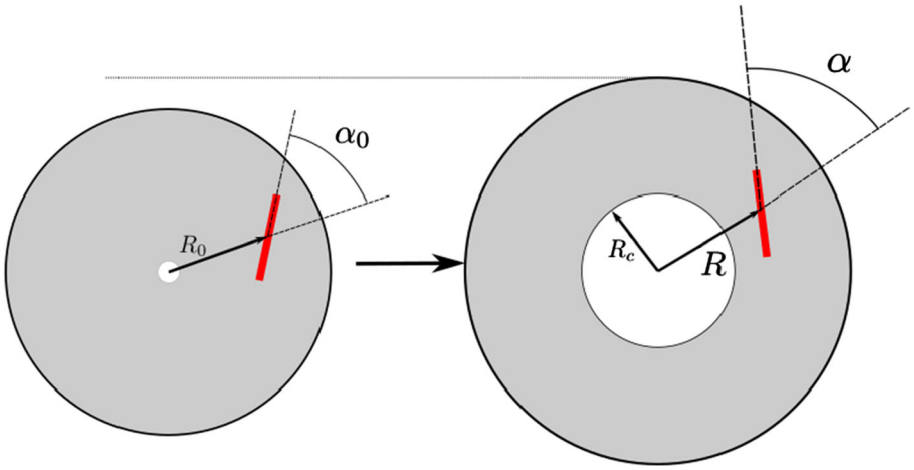

Fig. 9 The Shaayegan et al. model [60]. Note that the radius of the spherical envelope surrounding the fiber increases as the bubble grows

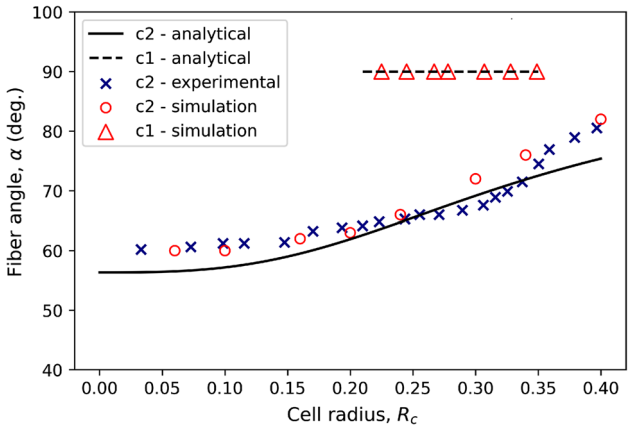

Fig. 10 Fiber angle α versus cell radius R_c: simulation results versus analytical and experimental data. In the legend c1 refers to case #1 and c2 refers to case #2, as described in Table 2. In both cases, the fiber consists of 10 particles with $k_s = k_b = 0.2$, and $\tau = 1$

conditions as specified in the table. For case 2, experimental data is also available [60].

As can be seen from Fig. 10, for case 1, the fiber only experiences radial translation, as expected and predicted by the analytical solution. In case 2, there is good agreement between the analytical model and the simulation data. Although both models predict the experimental data well, the LBM-MD-IBM model better predicts the trend in the experimental data because it is not limited by the simplifications of the analytical model, i.e., in case 2, α_0 is small, resulting in significant rotation of the fiber off its midpoint, which is not permitted by the analytical model.

3.4 Simulation results

The validation cases confirm that the model represents the correct physics. In this section, we showcase a number of simulations to demonstrate the capabilities of the model.

Note that the model is parallelized using the MPI library (details can be found in [7]). 2D simulations can be done on a desktop computer e.g., a 2D simulation of size 601×301 ($\approx 722k$ cells) with 250 fibers takes less than 1-hour to complete 10, 000 iterations on a six-core Intel i7 $8700K$. While it is possible to run 3D simulations on desktop CPUs, they benefit from fast compute nodes. On a 40-core compute node (Niagara supercomputer at the University of Toronto), a 3D simulation of size $101 \times 101 \times 101$ ($\approx 1m$ cells) takes about 30 minutes to complete 10, 000 iterations (excluding I/O).

We have used parameters in lattice units. In Appendix 1, we explain the conversion between dimensionless physical and lattice parameters in detail.

3.4.1 Foaming with fibers

Figures 11 and 12 show 2D and 3D foaming simulations with numerous rigid fibers of different lengths. The bubbles are randomly initialized with a disk-sampling algorithm as described in [7], and the fibers are randomly initialized with the help of the Bentley-Ottmann sweep line approach [62] so that they do not intersect with each other (in 3D, this is not needed, as the probability of two random fibers intersecting each other is insignificant). It can be seen that as the foam expands, the fibers interact with the bubbles and with each other, and ultimately settle in the walls between adjacent bubbles. Because of the two-way coupling of the MD and LBM solvers, the fibers also influence the foam structure. As shown in Fig. 11), the foam structure without fibers is different.

Performing such simulations can be very useful in practice. For example, the model can demonstrate the potential of foaming as a strategy to decrease the percolation threshold in conductive composite foams (CPCs). By analyzing the rotation and translation of fibers due to the interaction with bubbles, we can better understand how cell growth, void frac-

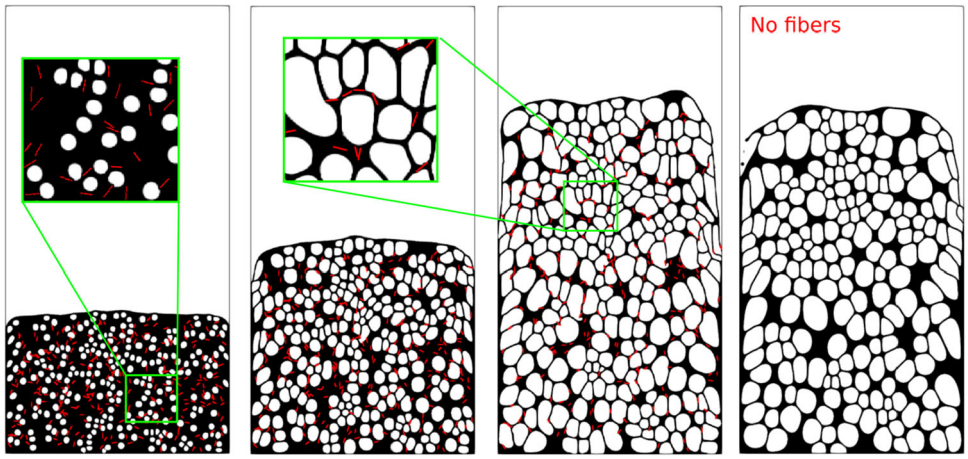

Fig. 11 Example of a 2D foaming simulation with 200 initial bubbles and 250 rigid fibers (shown in red). Note that some of the bubbles coalesce during the foaming process. Parameters: domain size 601×1201, $\tau = 0.9$, $\tau_g = 0.6$, $q = 1 \times 10^{-4}$, $k_\Pi = 8 \times 10^{-3}$ $k_s = k_b = 0.1$, $r_f = 10$, $10\delta x < L_f < 15\delta x$. The green boxes are zoomed in for a better view of the fibers. $t = 20 \times 10^2$ (left), $t = 50 \times 10^2$ (middle), $t = 92 \times 10^2$ (two rightmost images). The rightmost figure is of the same simulation without fibers. (Color figure online)

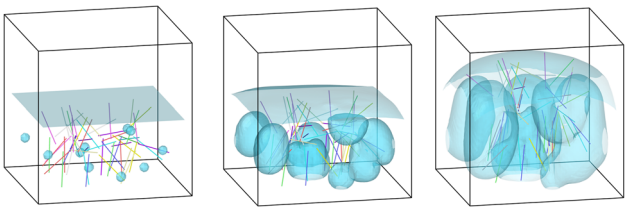

Fig. 12 Example of a 3D foaming simulation with 10 initial bubbles and 50 rigid fibers. Bubble interfaces are shown in blue. Note that some of the bubbles coalesce during the foaming process. Parameters: domain size $51 \times 51 \times 51$, $\tau = 1.0$, $\tau_g = 0.6$, $q = 4 \times 10^{-5}$, $k_\Pi = 8 \times 10^{-3}$ $k_s = k_b = 0.1$, $M = 10$, $r_f = 15$, $L_f = 12\delta x$. $t = 20 \times 10^2$ (left), $t = 50 \times 10^2$ (middle), $t = 92 \times 10^2$ (right). (Color figure online)

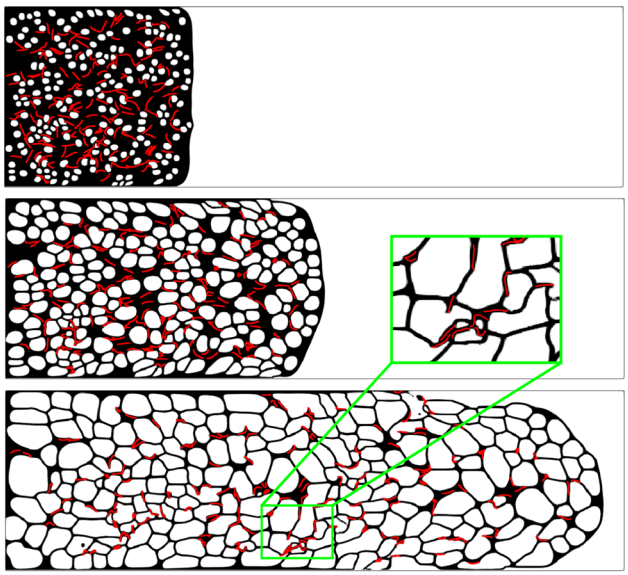

Fig. 13 Behavior of soft fibers during foaming with 200 initial nuclei, 250 fibers. *Parameters:* domain size 351×1201, $\tau = 1.0$, $\tau_g = 0.6$, $q = 2 \times 10^{-5}$, $k_\Pi = 8 \times 10^{-3}$ $k_s = 0.2$, $k_b = 0.0$, $M = 5$, $n_a = 20$, $25\delta x < L_f < 35\delta x$. $t = 16 \times 10^2$ (top), $t = 50 \times 10^2$ (middle), $t = 117 \times 10^2$ (bottom)

tion, and fiber size influence the percolation threshold (which is a nonlinear relationship [54,72]), and determine the proper void fraction that maximizes fiber interconnectivity (that is related to the electrical conductivity). In contrast to previous models (e.g., [60,73,74]), the model allows for the fluid flow and bubble dynamics to be physically modeled, it is not restricted to a small number of bubble and fibers, and bubble deformation is considered, which can lead to better prediction of important parameters such as percolation threshold in conductive polymer composites.

The model is also capable of simulating deformable fibers simply by setting $k_b = 0.0$. A 2D foaming simulation with deformable fibers is illustrated in Fig. 13. It can be seen that the deformability of the fibers can influence the foam structure and fiber connectivity. This capability is important as fillers are assumed to be rigid in available models [73,74], whereas in practice, fillers, such as MWCNTs, typically have low bending stiffness, causing fillers to curl and agglomerate, which can lead to lower fiber connectivity and thus foam conductivity [46,65,79].

The simulation of fiber breakage is enabled by setting $p^* > 0$ and specifying R_{max}. The same simulation as in Fig. 13 is seen in Fig. 14 with rigid fibers ($k_b = 0.2$), where $R_{max} = L_f/n_a * 1.05$ and $p^* = 0.8$, implying that there is a 80% chance that the bond between two particles i and j will break if its length exceeds 5% of its initial length. As the bubbles grow ($t = 300$ (left), $t = 1300$ (right)), some of

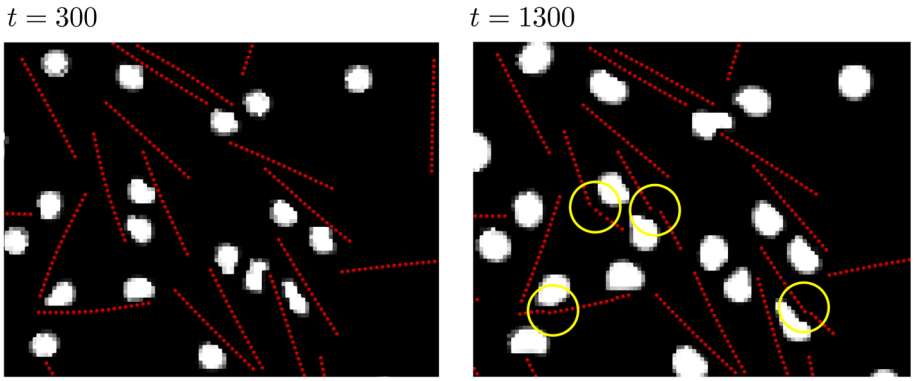

Fig. 14 Broken fibers are shown with yellow circles. Except for $R_{max} = L_f/n_a * 1.05$ and $p^* = 0.8$, the simulation parameters are similar to those of Fig. 13. $t = 300$ (left) $t = 1300$ (right). (Color figure online)

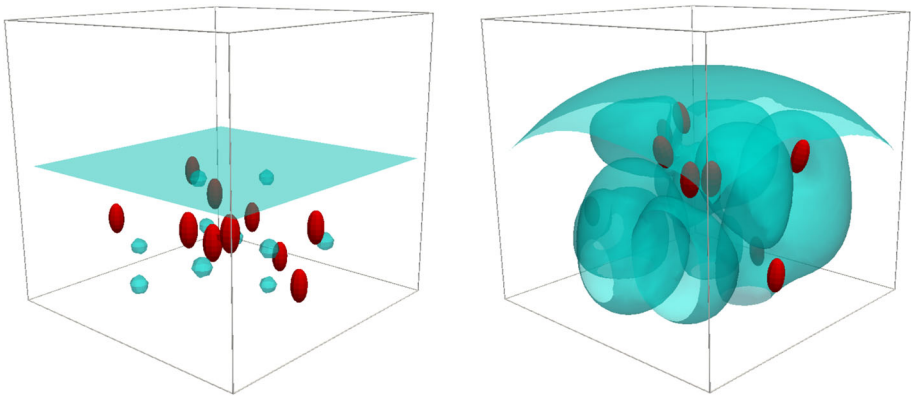

Fig. 15 3D foaming with rigid ellipsoid fillers (10 bubbles, 10 ellipsoids). *Parameters:* domain of size $101 \times 101 \times 101$, $\psi = 2$, $\kappa = 4$, $\tau = 0.95$, $\tau_g = 0.65$, $k_\Pi = 1 \times 10^{-2}$, $q = 2 \times 10^{-5}$, $M = 10$, $k_v = k_a = k_d = 2$, $k_b = k_s = 1$

the fibers break, under the stress of adjacent growing cells, as indicated by the yellow circles in Fig. 14 (right).

3.4.2 3D arbitrary-shaped fillers

In addition to fibers, other geometries can be used as fillers. Using the CG membrane model for 3D bodies introduced in Sect. 2.3.2, a foam expansion with 10 bubbles and 10 ellipsoid fillers is shown in Fig. 15 (bubble interfaces are shown in blue and the ellipsoid fillers are shown in red). Using 3D bodies can be useful in the study of solid fillers such as metallic particles and conducting polymer particles in foams [45]. There are no restrictions on using different filler geometries (e.g., different types of 3D bodies and fibers) in the same simulation.

4 Conclusion

A hybrid lattice Boltzmann/molecular dynamics model for the simulation of composite foams is presented, which is capable of simulating the foaming process (bubble growth, interaction, coalescence, etc.) as well as the interaction between the foam and fillers of different geometries such as fibers and arbitrarily-shaped 3D fillers. The LBM and MD models are coupled using a direct forcing immersed boundary method. The model can simulate the interaction of foams with rigid and deformable fillers, such as soft fibers, and can capture complex phenomena including fiber breakage.

Acknowledgements We thank the Natural Sciences and Engineering Research Council of Canada (NSERC) and Autodesk Inc. for their financial support. Computations were performed on the Niagara supercomputer at the SciNet HPC Consortium. SciNet is funded by: the Canada Foundation for Innovation; the Government of Ontario; Ontario Research Fund - Research Excellence; and the University of Toronto.

Appendix A: Conversion between dimensionless physical and lattice parameters

Dimensionless numbers are indicated with "*" superscript. Given a length scale δx, a timescale δt, a mass scale δm, and a substance scale δn, the following dimensionless numbers can be defined to convert lattice parameters to physical parameters, and vice versa.

$$\rho^* = \rho \frac{\delta x^3}{\delta m}$$
$$\nu^* = \rho \frac{\delta t}{\delta x^2}$$
$$q^* = \rho \frac{\delta x^3}{\delta n}$$
$$D^* = \rho \frac{\delta t}{\delta x^2}$$

$$\mathbf{g}^* = \mathbf{g}\frac{\delta t^2}{\delta x}$$
$$L_f^* = L_f\frac{1}{\delta x}$$
$$k_s^* = k_s\frac{\delta t^2}{\delta m}$$
$$k_b^* = k_b\frac{\delta t^2}{\delta m \delta x^2}$$
$$k_v^* = k_b\frac{\delta t^2}{\delta m \delta x^2}$$
$$k_d^* = k_d\frac{\delta t^2}{\delta m}$$
$$k_a^* = k_a\frac{\delta t^2}{\delta m}$$

where the dimensionless lattice parameters τ^* and τ_g^* are:

$$\tau^* = \frac{6\nu^* + 1}{2}$$
$$\tau_g^* = \frac{6D^* + 1}{2}$$

Note that because of the relationship between pressure, density, and the speed of sound ($p = \rho c_s^2$), for a given pressure and density δt and δx cannot be changed independently. Refer to "Koerner, et al. Springer Science & Business Media, 2008" for more details.

References

1. Adloo A, Sadeghi M, Masoomi M, Pazhooh HN (2016) High performance polymeric bipolar plate based on polypropylene/graphite/graphene/nano-carbon black composites for PEM fuel cells. Renew Energy 99:867–874
2. Advani SG, Tucker CL III (1987) The use of tensors to describe and predict fiber orientation in short fiber composites. J Rheol 31(8):751–784
3. Ameli A, Jung P, Park CB (2013) Electrical properties and electromagnetic interference shielding effectiveness of polypropylene/carbon fiber composite foams. Carbon 60:379–391
4. Ameli A, Jung P, Park CB (2013) Through-plane electrical conductivity of injection-molded polypropylene/carbon-fiber composite foams. Compos Sci Technol 76:37–44
5. Ameli A, Wang S, Kazemi Y, Park CB, Pötschke P (2015) A facile method to increase the charge storage capability of polymer nanocomposites. Nano Energy 15:54–65
6. Arefmanesh A, Advani SG, Michaelides EE (1990) A numerical study of bubble growth during low pressure structural foam molding process. Polym Eng Sci 30(20):1330–1337
7. Ataei M, Shaayegan V, Costa F, Han S, Park CB, Bussmann M (2021) LBfoam: an open-source software package for the simulation of foaming using the Lattice Boltzmann Method. Comput Phys Commun 259:107698
8. Ataei M, Shaayegan V, Wang C, Costa F, Han S, Park CB, Bussmann M (2019) Numerical analysis of the effect of the local variation of viscosity on bubble growth and deformation in polymer foaming. J Rheol 63(6):895–903
9. Bay RS, Tucker CL III (1992) Fiber orientation in simple injection moldings. Part I: theory and numerical methods. Polym Compos 13(4):317–331
10. Bay RS, Tucker CL III (1992) Fiber orientation in simple injection moldings. Part II: experimental results. Polym Compos 13(4):332–341
11. Bryning M, Islam MF, Kikkawa JM, Yodh A (2005) Very low conductivity threshold in bulk isotropic single-walled carbon nanotube-epoxy composites. Adv Mater 17:1186–1191
12. Chang E, Ameli A, Alian A, Mark LH, Yu K, Wang S, Park CB (2020) Percolation mechanism and effective conductivity of mechanically deformed 3-dimensional composite networks: Computational modeling and experimental verification. Compos Part B Eng 207:108552
13. Dang Z, Zheng M, Zha J (2016) 1D/2D carbon nanomaterial-polymer dielectric composites with high permittivity for power energy storage applications. Small 12(13):1688–701
14. Dao M, Li J, Suresh S (2006) Molecularly based analysis of deformation of spectrin network and human erythrocyte. Mater Sci Eng C 26(8):1232–1244
15. Favaloro AJ, Tseng HC, Pipes RB (2018) A new anisotropic viscous constitutive model for composites molding simulation. Compos Part A Appl Sci Manuf 115:112–122
16. Fedosov DA, Caswell B, Karniadakis GE (2010) A multiscale red blood cell model with accurate mechanics, rheology, and dynamics. Biophys J 98(10):2215–2225
17. Fedosov DA, Caswell B, Karniadakis GE (2010) Systematic coarse-graining of spectrin-level red blood cell models. Comput Methods Appl Mech Eng 199(29–32):1937–1948
18. Feng ZG, Michaelides EE (2002) Hydrodynamic force on spheres in cylindrical and prismatic enclosures. Int J Multiphase Flow 28(3):479–496
19. Feng ZG, Michaelides EE (2002) Interparticle forces and lift on a particle attached to a solid boundary in suspension flow. Phys Fluids 14(1):49–60
20. Feng ZG, Michaelides EE (2004) The immersed boundary-lattice Boltzmann method for solving fluid-particles interaction problems. J Comput Phys 195(2):602–628
21. Folgar F, Tucker CL III (1984) Orientation behavior of fibers in concentrated suspensions. J Reinf Plast Compos 3(2):98–119
22. Gawale A, Kulkarni A, Pratley M (2017) Multiscale modeling approach for short fiber reinforced plastic couplings. SAE Int J Mater Manuf 10(1):78–82
23. Genheden S, Essex JW (2015) A simple and transferable all-atom/coarse-grained hybrid model to study membrane processes. J Chem Theory Comput 11(10):4749–4759
24. Goldberg N, Ospald F, Schneider M (2017) A fiber orientation-adapted integration scheme for computing the hyperelastic tucker average for short fiber reinforced composites. Comput Mech 60(4):595–611
25. Guo Z, Shi B, Wang N (2000) Lattice BGK model for incompressible Navier–Stokes equation. J Comput Phys 165(1):288–306
26. Haghgoo M, Ansari R, Hassanzadeh-Aghdam M, Nankali M (2019) Analytical formulation for electrical conductivity and percolation threshold of epoxy multiscale nanocomposites reinforced with chopped carbon fibers and wavy carbon nanotubes considering tunneling resistivity. Compos Part A Appl Sci Manuf 126:105616
27. Hasheminejad SM, Sanaei R (2007) Effects of fiber ellipticity and orientation on dynamic stress concentrations in porous fiber-reinforced composites. Comput Mech 40(6):1015–1036
28. He X, Luo LS (1997) Lattice Boltzmann model for the incompressible Navier–Stokes equation. J Stat Phys 88(3):927–944
29. Inamuro T (2012) Lattice Boltzmann methods for moving boundary flows. Fluid Dyn Res 44(2):024001
30. Isaincu A, Dan M, Ungureanu V, Marşavina L (2021) Numerical investigation on the influence of fiber orientation mapping

procedure to the mechanical response of short-fiber reinforced composites using Moldflow, Digimat and Ansys software. In: Materials today: proceedings
31. Iwan A, Malinowski M, Paściak G (2015) Polymer fuel cell components modified by graphene: electrodes, electrolytes and bipolar plates. Renew Sustain Energy Rev 49:954–967
32. Jack DA, Schache B, Smith DE (2010) Neural network-based closure for modeling short-fiber suspensions. Polym Compos 31(7):1125–1141
33. Jeffery GB (1922) The motion of ellipsoidal particles immersed in a viscous fluid. Proc R Soc Lond Ser A Contain Pap Math Phys Character 102(715):161–179
34. Jewett AI, Stelter D, Lambert J, Saladi SM, Roscioni OM, Ricci M, Autin L, Maritan M, Bashusqeh SM, Keyes T et al (2021) Moltemplate: a tool for coarse-grained modeling of complex biological matter and soft condensed matter physics. J Mol Biol 433:166841
35. Jia L, Yan D, Yang Y, Zhou D, Cui C, Bianco E, Lou J, Vajtai R, Li B, Ajayan P, Li Z (2017) High strain tolerant EMI shielding using carbon nanotube network stabilized rubber composite. Adv Mater Technol 2:1700078
36. Kloss C, Goniva C, Hager A, Amberger S, Pirker S (2012) Models, algorithms and validation for opensource DEM and CFD-DEM. Prog Comput Fluid Dyn Int J 12(2–3):140–152
37. Köbler J, Schneider M, Ospald F, Andrä H, Müller R (2018) Fiber orientation interpolation for the multiscale analysis of short fiber reinforced composite parts. Comput Mech 61(6):729–750
38. Lyu J, Zhao X, Hou X, Zhang Y, Li T, Yan Y (2017) Electromagnetic interference shielding based on a high strength polyaniline-aramid nanocomposite. Compos Sci Technol 149:159–165
39. Mao W, Alexeev A (2014) Motion of spheroid particles in shear flow with inertia. J Fluid Mech 749:145
40. Martin JJ, Riederer MS, Krebs MD, Erb RM (2015) Understanding and overcoming shear alignment of fibers during extrusion. Soft Matter 11(2):400–405
41. Montgomery-Smith S, Jack D, Smith DE (2011) The fast exact closure for Jeffery's equation with diffusion. J Non-Newton Fluid Mech 166(7–8):343–353
42. Okamoto M, Nam PH, Maiti P, Kotaka T, Nakayama T, Takada M, Ohshima M, Usuki A, Hasegawa N, Okamoto H (2001) Biaxial flow-induced alignment of silicate layers in polypropylene/clay nanocomposite foam. Nano Lett 1(9):503–505
43. Oliveira M, Sayeg IJ, Ett G, Antunes R (2014) Corrosion behavior of polyphenylene sulfide-carbon black-graphite composites for bipolar plates of polymer electrolyte membrane fuel cells. Int J Hydrogen Energy 39:16405–16418
44. Pang H, Xu L, Yan D, Li Z (2014) Conductive polymer composites with segregated structures. Prog Polym Sci 39:1908–1933
45. Pang H, Xu L, Yan DX, Li ZM (2014) Conductive polymer composites with segregated structures. Prog Polym Sci 39(11):1908–1933
46. Payandehpeyman J, Mazaheri M, Khamehchi M (2020) Prediction of electrical conductivity of polymer-graphene nanocomposites by developing an analytical model considering interphase, tunneling and geometry effects. Compos Commun 21:100364
47. Peskin CS (1977) Numerical analysis of blood flow in the heart. J Comput Phys 25(3):220–252
48. Pivkin IV, Karniadakis GE (2008) Accurate coarse-grained modeling of red blood cells. Phys Rev Lett 101(11):118105
49. Plimpton S (1995) Fast parallel algorithms for short-range molecular dynamics. J Comput Phys 117(1):1–19
50. Radzuan NAM, Sulong AB, Sahari J (2017) A review of electrical conductivity models for conductive polymer composite. Int J Hydrogen Energy 42:9262–9273
51. Rahman WAWA, Sin LT, Rahmat AR (2008) Injection moulding simulation analysis of natural fiber composite window frame. J Mater Process Technol 197(1–3):22–30
52. Reasor DA Jr, Clausen JR, Aidun CK (2012) Coupling the lattice-Boltzmann and spectrin-link methods for the direct numerical simulation of cellular blood flow. Int J Numer Methods Fluids 68(6):767–781
53. Ren F, Shi Y, Ren P, Si X, Wang H (2017) Cyanate ester resin filled with graphene nanosheets and NiFe2O4 reduced graphene oxide nanohybrids for efficient electromagnetic interference shielding. Nano 12:1750066
54. Rizvi R, Naguib H (2013) Porosity and composition dependence on electrical and piezoresistive properties of thermoplastic polyurethane nanocomposites. J Mater Res 28(17):2415
55. Sandler JKW, Kirk JE, Kinloch I, Shaffer M, Windle A (2003) Ultra-low electrical percolation threshold in carbon-nanotube-epoxy composites. Polymer 44:5893–5899
56. Sasayama T, Inagaki M (2017) Simplified bead-chain model for direct fiber simulation in viscous flow. J Non-Newton Fluid Mech 250:52–58
57. Schwarz S, Kempe T, Fröhlich J (2015) A temporal discretization scheme to compute the motion of light particles in viscous flows by an immersed boundary method. J Comput Phys 281:591–613
58. Seil P, Pirker S (2016) LBDEMcoupling: open-source power for fluid-particle systems. In: International conference on discrete element methods, pp 679–686. Springer
59. Semlali Aouragh Hassani FZ, Ouarhim W, Zari N, Bensalah MO, Rodrigue D, Bouhfid R, Qaiss Aek (2019) Injection molding of short coir fiber polypropylene biocomposites: prediction of the mold filling phase. Polym Compos 40(10):4042–4055
60. Shaayegan V, Ameli A, Wang S, Park CB (2016) Experimental observation and modeling of fiber rotation and translation during foam injection molding of polymer composites. Compos Part A Appl Sci Manuf 88:67–74
61. Shokri P, Bhatnagar N (2007) Effect of packing pressure on fiber orientation in injection molding of fiber-reinforced thermoplastics. Polym Compos 28(2):214–223
62. Smid M (2003) Computing intersections in a set of line segments: the Bentley–Ottmann algorithm
63. Tan J, Sinno TR, Diamond SL (2018) A parallel fluid-solid coupling model using LAMMPS and Palabos based on the immersed boundary method. J Comput Sci 25:89–100
64. Tang H, Wang P, Zheng P, Liu X (2016) Core-shell structured $BaTiO_3$ polymer hybrid nanofiller for poly(arylene ether nitrile) nanocomposites with enhanced dielectric properties and high thermal stability. Compos Sci Technol 123:134–142
65. Tang ZH, Li YQ, Huang P, Fu YQ, Hu N, Fu SY (2021) A new analytical model for predicting the electrical conductivity of carbon nanotube nanocomposites. Compos Commun 23:100577
66. Tran MP, Detrembleur C, Alexandre M, Jerome C, Thomassin JM (2013) The influence of foam morphology of multi-walled carbon nanotubes/poly (methyl methacrylate) nanocomposites on electrical conductivity. Polymer 54(13):3261–3270
67. Tschisgale S, Kempe T, Fröhlich J (2018) A general implicit direct forcing immersed boundary method for rigid particles. Comput Fluids 170:285–298
68. Van Der Spoel D, Lindahl E, Hess B, Groenhof G, Mark AE, Berendsen HJ (2005) GROMACS: fast, flexible, and free. J Comput Chem 26(16):1701–1718
69. Wang C, Shaayegan V, Ataei M, Costa F, Han S, Bussmann M, Park CB (2019) Accurate theoretical modeling of cell growth by comparing with visualized data in high-pressure foam injection molding. Eur Polym J 119:189–199
70. Wang, J, Jin X (2010) Comparison of recent fiber orientation models in Autodesk Moldflow insight simulations with measured fiber orientation data. In: Polymer processing society 26th annual meeting. Citeseer

71. Wang J, O'Gara JF, Tucker CL III (2008) An objective model for slow orientation kinetics in concentrated fiber suspensions: theory and rheological evidence. J Rheol 52(5):1179–1200
72. Wang S, Ameli A, Shaayegan V, Kazemi Y, Huang Y, Naguib H, Park CB (2018) Modelling of rod-like fillers' rotation and translation near two growing cells in conductive polymer composite foam processing. Polymers 10(3):261. https://www.mdpi.com/2073-4360/10/3/261
73. Wang S, Huang Y, Chang E, Zhao C, Ameli A, Naguib HE, Park CB (2021) Evaluation and modeling of electrical conductivity in conductive polymer nanocomposite foams with multiwalled carbon nanotube networks. Chem Eng J 411:128382
74. Wang S, Huang Y, Zhao C, Chang E, Ameli A, Naguib H, Park CB (2020) Theoretical modeling and experimental verification of percolation threshold with MWCNTs' rotation and translation around a growing bubble in conductive polymer composite foams. Compos Sci Technol 199:108345
75. Yamamoto S, Matsuoka T (1993) A method for dynamic simulation of rigid and flexible fibers in a flow field. J Chem Phys 98(1):644–650
76. Yamamoto S, Matsuoka T (1995) Dynamic simulation of fiber suspensions in shear flow. J Chem Phys 102(5):2254-2260
77. Yarin A, Gottlieb O, Roisman I (1997) Chaotic rotation of triaxial ellipsoids in simple shear flow. J Fluid Mech 340:83–100
78. Yu A, Pak AJ, He P, Monje-Galvan V, Casalino L, Gaieb Z, Dommer AC, Amaro RE, Voth GA (2021) A multiscale coarse-grained model of the SARS-CoV-2 virion. Biophys J 120(6):1097–1104
79. Zare Y, Rhee KY (2017) A simple methodology to predict the tunneling conductivity of polymer/CNT nanocomposites by the roles of tunneling distance, interphase and CNT waviness. RSC Adv 7(55):34912–34921
80. Zhao B, Zhao C, Li R, Hamidinejad SM, Park CB (2017) Flexible, ultrathin, and high-efficiency electromagnetic shielding properties of Poly(Vinylidene Fluoride)/Carbon composite films. ACS Appl Mater Interfaces 9(24):20873–20884
81. Zhao C, Mark LH, Kim S, Chang E, Park CB, Lee PC (2021) Recent progress in micro-/nano-fibrillar reinforced polymeric composite foams. Polym Eng Sci 61(4):926–941. https://doi.org/10.1002/pen.25643